Full-polarized Tomographic Diffraction Microscopy Achieves a Resolution about One-Fourth of the Wavelength

T. Zhang,[1] Y. Ruan,[1] G. Maire,[1] D. Sentenac,[3] A. Talneau,[2] K. Belkebir,[1] P. C. Chaumet,[1,*] and A. Sentenac[1]

[1]*Aix Marseille Université, CNRS, Centrale Marseille, Institut Fresnel, UMR 7249, 13013 Marseille, France*
[2]*Laboratoire de Photonique et de Nanostructure, 91460 Marcoussis, France*
[3]*European Gravitational Observatory, 56021 Cascina (PI), Italy*

We present a marker-free microscope that records the phase, amplitude, and polarization state of the field diffracted by the sample for different illumination directions. The data are processed with an appropriate inversion method to yield the sample permittivity map. We observe that the full-polarized information ameliorates significantly the three-dimensional image of weakly scattering subdiffraction objects. A resolution about one-fourth of the illumination wavelength is experimentally demonstrated on complex samples.

Optical microscopy is an old, popular tool for imaging microscopic samples. In the past decades, many different configurations such as confocal, dark-field, phase [1] or the more recent tomographic diffraction [2] microscopies have been developed to improve the resolution, the sensitivity, and/or the contrast of nonfluorescent specimen images. All these techniques rely on the same physical principle: the sample interacts with an incident light beam (coherent or incoherent) and the image is formed analogically or numerically from the scattered far field. In the single scattering regime, a far-field microscope is ideally able to capture the sample information up to frequency $2/\lambda$ where λ is the illumination wavelength [3]. Thus, the resolution, defined as the full width at half maximum of the image of a point object, could, theoretically, reach $\lambda/4$, i.e., half the conventional diffraction limit. In practice, the noise and the image formation process deteriorate the restitution of the sample high spatial frequencies. Therefore, the resolution of the best current microscopes is still about $\lambda/2$ [4].

A promising way for ameliorating the resolution is to take advantage of the vectorial nature of light. Thus, the polarization-dependent behavior of a tightly focused beam [5,6] has been used to improve the resolution of a confocal-like microscope along one specific direction [7]. However, the intrinsic difficulty to combine confocal images obtained under various incident polarization states [7] has hampered the use of this approach to reach a resolution significantly beyond the diffraction limit in all directions of the image plane.

Another interesting approach is tomographic diffraction microscopy (TDM) which numerically reconstructs the sample three-dimensional image from many holograms recorded under different incident angles. Remarkably, a transverse resolution about one-fourth of the wavelength has been observed on elongated objects [8] with TDM. Yet, this achievement has never been evidenced on a three-dimensional specimen. The most likely reason is that

TDM does not account for the light polarization effect in the image formation process [9]. The holograms are obtained for one given polarization state and the reconstruction procedures are based on scalar approximate models [4,10,11].

In this Letter, we sought to exploit the full potential of TDM by taking advantage of the light polarization. We implemented a tomographic diffraction microscope that records and processes the vectorial complex field scattered by a sample for any incident polarization state [12]. The setup, described in Fig. 1, is a modified reflection microscope in which an off-axis holography technique has been introduced to recover the phase and amplitude of the field at the microscope image plane. A collimated laser beam (He-Ne wavelength $\lambda = 633$ nm), controlled by a mirror mounted on step motors (Newport NSA12), illuminates the sample through an air objective satisfying Sine-Abbe condition with numerical aperture NA = 0.95 (Zeiss
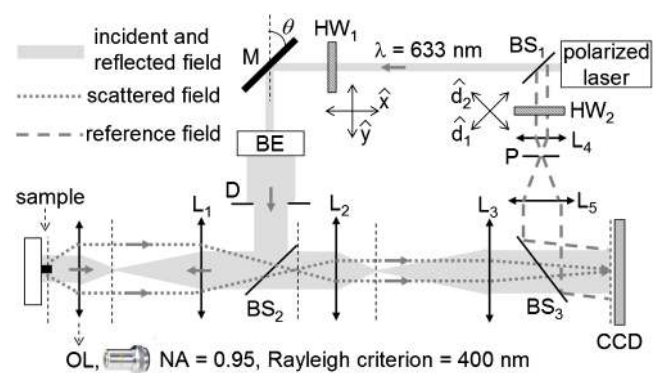

FIG. 1 (color online).   Schematic of the full-polarized TDM setup. M the rotative mirror. BE the beam expander. *D* the diaphragm. BS the beam splitter. OL the objective lens. *P* the pinhole. L_1 the tube lens. L_2 and L_3 are the relay lenses ($f' = 3.5$ and 20 cm, respectively). HW$_1$ and HW$_2$ the half-wave plate on the incident field and reference field, respectively.

Epiplan-Apochromat ×50) under various angles of inci-
dence. At the image plane of the microscope, the field
scattered by the sample, E, reads, overlooking the magni-
fication factor,

$$\mathbf{E}(\mathbf{r}_\parallel) = \int_{k_\parallel < k_0 \mathrm{NA}} \frac{1}{\gamma}(e_s \hat{\mathbf{s}} + e_p \hat{\mathbf{p}}) \exp(i\mathbf{k}_\parallel . \mathbf{r}_\parallel) \mathrm{d}\mathbf{k}_\parallel, \quad (1)$$

where $\hat{\mathbf{z}}$ denotes the optical axis of the microscope,
$\gamma = \sqrt{(2\pi/\lambda)^2 - k_\parallel^2}$, $\hat{\mathbf{s}} = \hat{\mathbf{z}} \times \hat{\mathbf{k}}$, $\hat{\mathbf{p}} = \hat{\mathbf{s}} \times \hat{\mathbf{k}}$ with $\mathbf{k} = \mathbf{k}_\parallel + \gamma\hat{\mathbf{z}}$ and (e_s, e_p) are the s and p complex amplitudes
of the sample scattered plane wave propagating along $\mathbf{k}$.
For each illumination, one records with a CCD camera
(Kappa DX4-1020FW), the interference patterns between
E and an off-axis reference wave which is successively
polarized along two different directions $\hat{\mathbf{d}}_1$ and $\hat{\mathbf{d}}_2$ [13].
Processing the holograms yields $\mathbf{E}.\hat{\mathbf{d}}_1$ and $\mathbf{E}.\hat{\mathbf{d}}_2$ from
which (e_s, e_p) for all $\mathbf{k}_\parallel$ such that $k_\parallel < k_0 \mathrm{NA}$ are easily
extracted. To obtain the vectorial complex field scattered
by the sample for any incident polarization state, one needs
to record (e_s, e_p) for two independent incident polarization
states. Hence, the full-polarized TDM mode requires four
intensity measurements for each incident angle (and pos-
sibly only two using [12]).

The different incident and reference polarization states
are formed thanks to the half-wave plates that are placed on
the illumination and reference wave paths, see Fig. 1. To
avoid turning off the specular reflection (which is used for
normalizing the data [14]), the incident polarization direc-
tions are set to $\hat{\mathbf{x}}$ and $\hat{\mathbf{y}}$, while the reference ones are $\hat{\mathbf{d}}_1 = (\hat{\mathbf{x}} + \hat{\mathbf{y}})/\sqrt{2}$ and $\hat{\mathbf{d}}_2 = (\hat{\mathbf{x}} - \hat{\mathbf{y}})/\sqrt{2}$. For comparison pur-
poses, we also considered the classical implementation of
TDM in which the incident and reference polarization
directions are the same, either $\hat{\mathbf{x}}$ or $\hat{\mathbf{y}}$. In these configura-
tions (hereafter indicated by $\hat{\mathbf{x}}\hat{\mathbf{x}}$ or $\hat{\mathbf{y}}\hat{\mathbf{y}}$), the data consist of
the scalar projection of the scattered field on the incident
polarization state. Thus, there are four times less data in the
$\hat{\mathbf{x}}\hat{\mathbf{x}}$ or $\hat{\mathbf{y}}\hat{\mathbf{y}}$ modes than in the full-polarization mode.

In this Letter, the samples to be imaged are deposited on
a silicon substrate and are described by a relative permit-
tivity contrast $\chi(\mathbf{r})$ with respect to the planar geometry
[9,15]. The unknown sample permittivity contrast is recon-
structed from the TDM data using an iterative inversion
method based on a rigorous vectorial electromagnetic
model of the scattered far field (e_s, e_p), which, in particu-
lar, accounts for the substrate [16]. The algorithm consists
in estimating, iteratively, the relative permittivity contrast
χ of a bounded domain W (which is known to contain the
sample), such that it minimizes a cost function representing
the distance between the measurements and the simulated
scattered far field obtained with the permittivity estimation
[9,17]. The minimization of the cost function is performed
using a conjugate gradient algorithm and, to improve the
reconstruction, the unknown relative permittivity in W is
assumed to be real and positive. Note that the method is

adapted to any TDM data. In the full-polarization mode,
the cost function involves the full vectorial field scattered
by the sample, whereas in the $\hat{\mathbf{x}}\hat{\mathbf{x}}$ mode, it involves only
the projection of the scattered field.

For investigating the performance of our setup, we con-
sider a sample made of $h = 150$ nm high resin cylinders
with diameter $D = 150$ nm and relative permittivity 2
deposited on a planar Si substrate of relative permittivity
$15 + i0.15$, and centered at the summits of a square with
sides 300 nm along $\hat{\mathbf{x}}$ and $\hat{\mathbf{y}}$ as depicted in Fig. 2(a). The
scattered far field is measured in both the full-polarized and
scalar ($\hat{\mathbf{x}}\hat{\mathbf{x}}$, $\hat{\mathbf{y}}\hat{\mathbf{y}}$) modes for 10 incident directions in the
(x, z) plane and 10 in the (y, z) plane with azimuthal angles
varying from $-50°$ to $50°$. With this angular configuration,
the diffraction limit of the microscope is about $0.5\lambda/\mathrm{NA} \approx 340$ nm, i.e., above the cylinders center interdistance. It is
observed in Fig. 2(b) that, unsurprisingly, the four cylin-
ders cannot be distinguished on a classical wide-field
microscope image (which was synthesized by summing
the image field intensities for all the illuminations).

We first analyze the achievement of a classical TDM
implementation by processing the scalar $\hat{\mathbf{y}}\hat{\mathbf{y}}$ data with the
usual inverse Fourier transform algorithm [2]. The latter
relies on a scalar, free-space (no substrate), single scatter-
ing model which states that the far field scattered in the $\mathbf{k}$
direction by a sample illuminated by a plane wave with
wave vector $\mathbf{k}_i$ is proportional to the three-dimensional
Fourier transform of $\chi(\mathbf{r})$ taken at $(\mathbf{k} - \mathbf{k}_i)$. Theoretically,
in a noise-free configuration, the transverse image resolu-
tion should be about $0.25\lambda/\mathrm{NA} \approx 170$ nm with our angle
configuration, i.e., below the cylinders center interdistance
[3]. Yet, it is seen in Fig. 3(a) that the simple inversion
scheme fails in retrieving the sample. Its noise sensitivity
(due to the weak number of incidences) and its model
errors are prohibitive for imaging such small objects.

Applying the iterative inversion method to the same
scalar data provides a much better sample estimate. The
cylinders height is now accurately retrieved. However,
their shapes are strongly elongated along the $\hat{\mathbf{x}}$ axis,
Fig. 3(b). This resolution anisotropy is a direct conse-
quence of the incident and reference polarization choice,
as was observed in Ref. [7], and will be explained below.
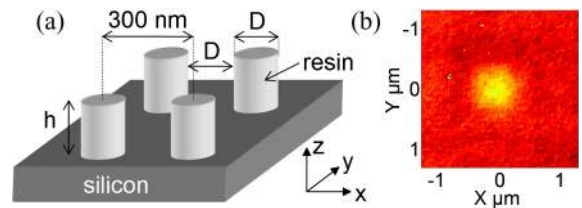We now turn to the reconstructions obtained either with the

FIG. 2 (color online). (a) Sample geometry. $D = 150$ nm and
$h = 150$ nm. (b) Wide-field image of the sample obtained using
spatially incoherent illumination: details of the object are not
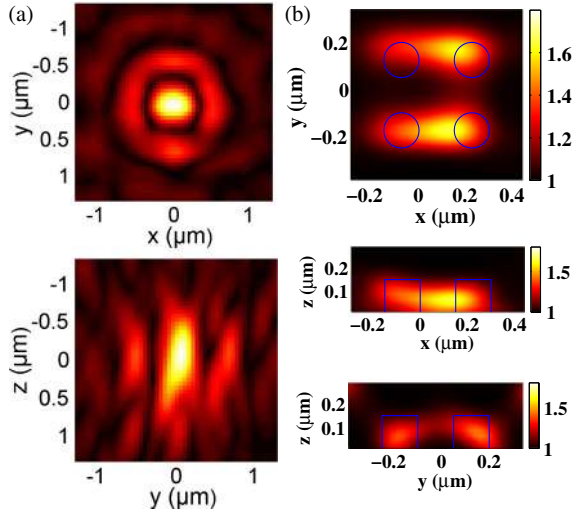resolved.

FIG. 3 (color online).   Sample reconstructions obtained from the scalar $\hat{\mathbf{y}}\,\hat{\mathbf{y}}$ data. (a) Longitudinal and transverse cuts of the three-dimensional image given by a direct inversion method based on a free-space scalar model. (b) Longitudinal and transverse cuts of the relative permittivity estimation ($\varepsilon = \chi + 1$) given by an iterative inversion method based on a rigorous vectorial model of the data accounting for the substrate and for the field projection onto the $\hat{\mathbf{y}}$ direction.

combined scalar $\hat{\mathbf{x}}\,\hat{\mathbf{x}}$ and $\hat{\mathbf{y}}\,\hat{\mathbf{y}}$ data, Figs. 4(a)–4(c), or the full-polarized vectorial mode, Figs. 4(d)–4(f). In both cases, the four cylinders are accurately retrieved with isotropic resolution, the full-polarized vectorial data yielding
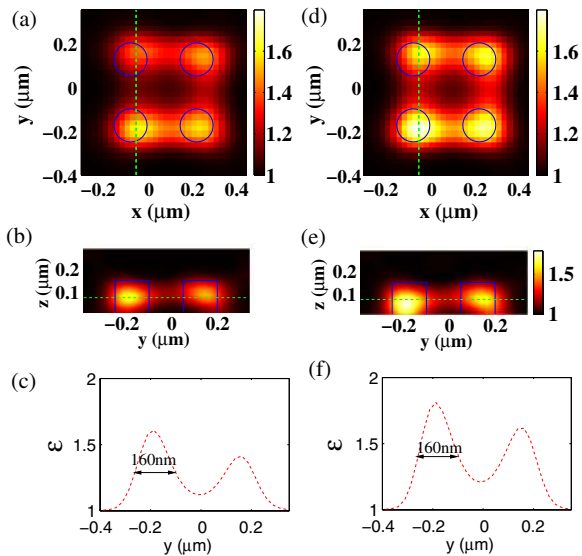

FIG. 4 (color online).   Relative permittivity reconstructions, $\varepsilon = \chi + 1$, obtained by the iterative inversion method based on a rigorous vectorial model of the field from the combined $\hat{\mathbf{x}}\,\hat{\mathbf{x}}$ and $\hat{\mathbf{y}}\,\hat{\mathbf{y}}$ data (a)–(c) and from the full-polarized vectorial data (d)–(f). (a),(d) xy section, (b),(e) yz section taken along the dashed line in (a),(d), (c),(f) reconstructed permittivity along the dashed line in (b),(e). The full width at half maximum of the reconstructed permittivity is about one-fourth of the wavelength.

a better quantitative estimation of the permittivity level. The resolution, defined as the full width at half maximum of the reconstructed permittivity peaks, Figs. 4(c) and 4(f), is about one-fourth of the wavelength.

The role of the incident and reference polarization states on the image resolution requires a careful analysis. Indeed, when single scattering is dominant (which is the case for this sample), the scalar $\hat{\mathbf{x}}\,\hat{\mathbf{x}}$ or $\hat{\mathbf{y}}\,\hat{\mathbf{y}}$ data give access to the sample permittivity Fourier coefficients within the same Fourier domain as the vectorial full-polarized data [15]. Hence, the resolution of the image depends only on the ability to extract, from noisy data, the permittivity Fourier coefficients at the highest accessible spatial frequencies. The latter are conveyed by the far field scattered at high angles, namely for large $\mathbf{k} - \mathbf{k}_i$. Now, in presence of a substrate, the far-field behavior in these directions significantly differs depending on the incident polarization state. In Fig. 5, we plot the scattered far-field modulus in the $\mathbf{k}_{\parallel}$ plane obtained experimentally and theoretically when the sample is illuminated under $50°$ in the (x, z) plane with a p-polarized (corresponding to the $\hat{\mathbf{x}}$ direction for the incident half-wave plate) and s-polarized (corresponding to the $\hat{\mathbf{y}}$ direction) plane waves. We observe that the back scattered field is about twice bigger with the p-polarized incident wave than with the s-polarized incident wave. The better signal to noise ratio at high angles obtained with p-polarized incident waves explains the better resolution along the $\hat{\mathbf{y}}$ direction that is observed in Fig. 3(b). To confirm this interpretation, we plot, in Fig. 6, the relative permittivity map reconstructed by the iterative inversion
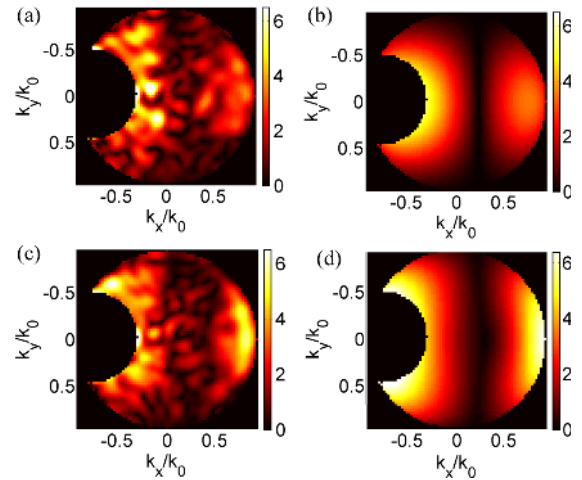

FIG. 5 (color online).   Experimental (a),(c) and theoretical (b), (d) modulus of the far field scattered by the sample illuminated in the (x, z) plane under $50°$ of incidence. The scattered field is normalized by the incident magnitude times 10^8. The black disk on the left indicates the nonexploitable angular domain about the specular reflection. (a),(b) the incident wave is s polarized. (c), (d) the incident wave is p polarized. One observes on the right of the plots that the back scattered field amplitudes, which convey the highest spatial frequency sample information, are twice as big in p polarization as in s polarization.
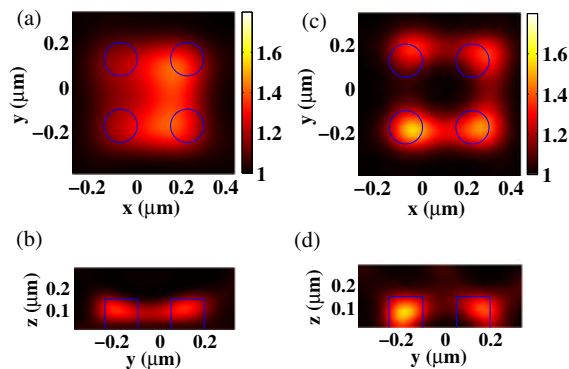
FIG. 6 (color online). *xy* (a),(c) and *yz* (b),(d) sections of the reconstructed permittivity given by the iterative "rigorous" inversion method from the measured far field. (a) and (b) with *s*-polarized incident waves; (c) and (d) with *p*-polarized incident waves. The superiority of *p* illumination for imaging the sample is evidenced.

method from the scattered vectorial field obtained using only *s*-polarized incident waves, Figs. 6(a) and 6(b), or only *p*-polarized incident waves, Figs. 6(c) and 6(d). As expected, the *p*-polarized mode yields an accurate sample reconstruction, similar to that of the full-polarized mode, while the *s*-polarized mode provides a totally blurred image.

To document further the potential of the full-polarized TDM, we image a complex sample made of twelve resin rods of width 100 nm, length 300 nm, and height 140 nm radially placed at the summit of a dodecagon [Fig. 7(a)]. The sample is illuminated by eight directions of incidence, defined by a fixed polar angle $\theta = 60°$ and an azimuthal angle regularly spaced within 2π. The dark-field microscope image, simulated by summing the scattered
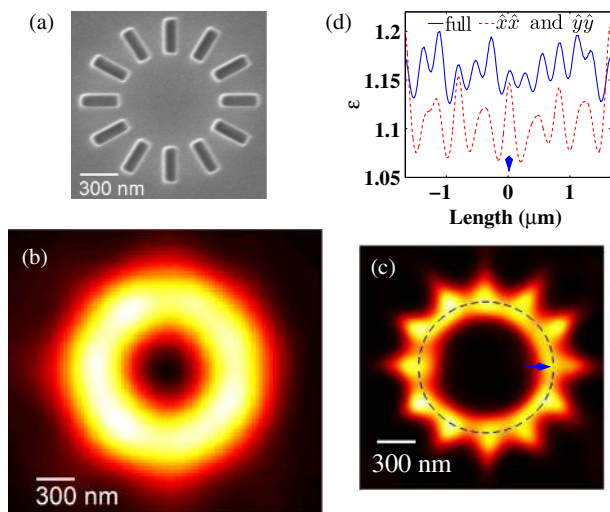

FIG. 7 (color online). (a) Scanning electron microscope image. (b) Dark-field optical microscope image. (c) Reconstructed permittivity averaged over the sample's height using full-polarized TDM data. (d) Permittivity along the dashed circle in (c). Plain line: full-polarized data; dashed line: the combined $\hat{x}\hat{x}$ and $\hat{y}\hat{y}$ data.

intensities recorded at the image plane for all the illuminations, displays a blurred ring with no indication of individual rods [Fig. 7(b)]. In contrast, the full polarized TDM recovers the twelve rods, Fig. 7(c). The reconstructed permittivity taken along a circle passing through the middle of the rods demonstrates that the technique is able to distinguish the rods whatever their orientation even though their interdistance is about one-fourth of the wavelength. On this complex sample, the full-polarized permittivity reconstruction is significantly better than the $\hat{x}\hat{x}$ and $\hat{y}\hat{y}$ one, Fig. 7(d), especially for the rods on either side of the image diagonals.

In conclusion, we have developed the first optical digital microscope that exploits all the information accessible via the diffraction process (intensity, phase, and polarization state of the scattered field for any possible illumination within the numerical aperture of the objective). In the single scattering regime, this ultimate microscope is able to reconstruct permittivity maps with a resolution about one-fourth of the wavelength. This experimental achievement, which outperforms that of all existing far-field microscopes, points out the importance of accounting for light polarization when tackling super resolution and sets a landmark in optical far-field imaging.

*patrick.chaumet@fresnel.fr
[1] D. B. Murphy and M. W. Davidson, *Fundamentals of Light Microscopy and Electronic Imaging* (Wiley, New York, 2012).
[2] V. Lauer, J. Microsc. **205**, 165 (2002).
[3] O. Haeberlé, K. Belkebir, H. Giovaninni, and A. Sentenac, J. Mod. Opt. **57**, 686 (2010).
[4] Y. Cotte, F. Toy, P. Jourdain, N. Pavillon, D. Boss, P. Magistretti, P. Marquet, and C. Depeursinge, Nat. Photonics **7**, 113 (2013).
[5] R. Dorn, S. Quabis, and G. Leuchs, Phys. Rev. Lett. **91**, 233901 (2003).
[6] D. Lara and C. Dainty, Appl. Opt. **45**, 1917 (2006).
[7] K. A. Serrels, E. Ramsay, R. J. Warburton, and D. T. Reid, Nat. Photonics **2**, 311 (2008).
[8] G. Maire, F. Drsek, J. Girard, H. Giovannini, A. Talneau, D. Konan, K. Belkebir, P. C. Chaumet, and A. Sentenac, Phys. Rev. Lett. **102**, 213905 (2009).
[9] Y. Ruan, P. Bon, E. Mudry, G. Maire, P. C. Chaumet, H. Giovannini, K. Belkebir, A. Talneau, B. Wattellier, S. Monneret et al., Opt. Lett. **37**, 1631 (2012).
[10] Y. Sung, W. Choi, C. Fang-Yen, K. B. Zadegan, R. R. Dasari, and M. S. Feld, Opt. Express **17**, 266 (2009).
[11] W. Choi, C. Fang-Yen, K. Badizadegan, S. Oh, N. Lue, R. R. Dasari, and M. S. Feld, Nat. Methods **4**, 717 (2007).
[12] T. Colomb, F. Dürr, E. Cuche, P. Marquet, H. G. Limberger, R.-P. Salathé, and C. Depeursinge, Appl. Opt. **44**, 4461 (2005).
[13] The experiment was automatized using the free software OPTICSBENCHUI, http://www.opticsbenchui.com/.

P H Y S I C A L   R E V I E W   L E T T E R S

[14] G. Maire, J. Girard, F. Drsek, H. Giovannini, A. Talneau, K. Belkebir, P. C. Chaumet, and A. Sentenac, J. Mod. Opt. **57,** 746 (2010).

[15] E. Mudry, P. C. Chaumet, K. Belkebir, G. Maire, and A. Sentenac, Opt. Lett. **35,** 1857 (2010).

[16] K. Belkebir, P. C. Chaumet, and A. Sentenac, J. Opt. Soc. Am. A **22,** 1889 (2005).

[17] E. Mudry, P. C. Chaumet, K. Belkebir, and A. Sentenac, Inverse Probl. **28,** 065007 (2012).